

Supplementary Information for

Impact of the electrode conductivity on the electrolyte interfacial structuring and its implications to the Na^{0/+} electrochemical performance

Dmitrii A. Rakov^{1,2}, Ju Sun¹, Pavel V. Cherepanov³, Khryslyn Arano¹, Patrick C. Howlett^{1,2},
Alexandr N. Simonov³, Fangfang Chen^{1,2*}, Maria Forsyth^{1,2*}*

¹Institute for Frontier Materials, Deakin University, Geelong, Victoria 3217, Australia

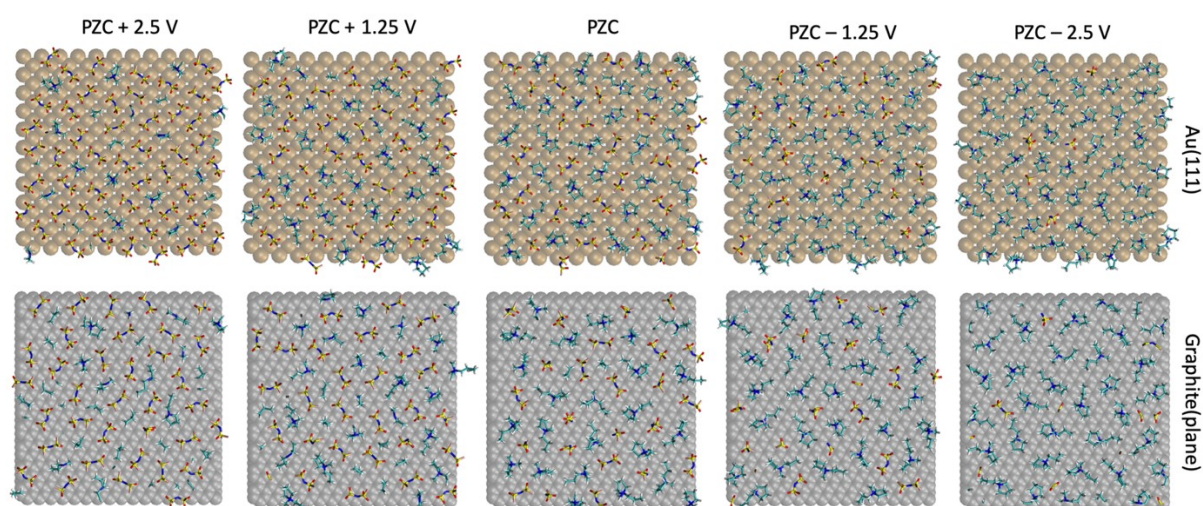
²ARC Centre of Excellence for Electromaterials Science (ACES), Deakin University, Burwood, Victoria 3125, Australia

³School of Chemistry, Monash University and the ARC Centre of Excellence for Electromaterials Science, Clayton, 3800, Australia.

*Corresponding authors.

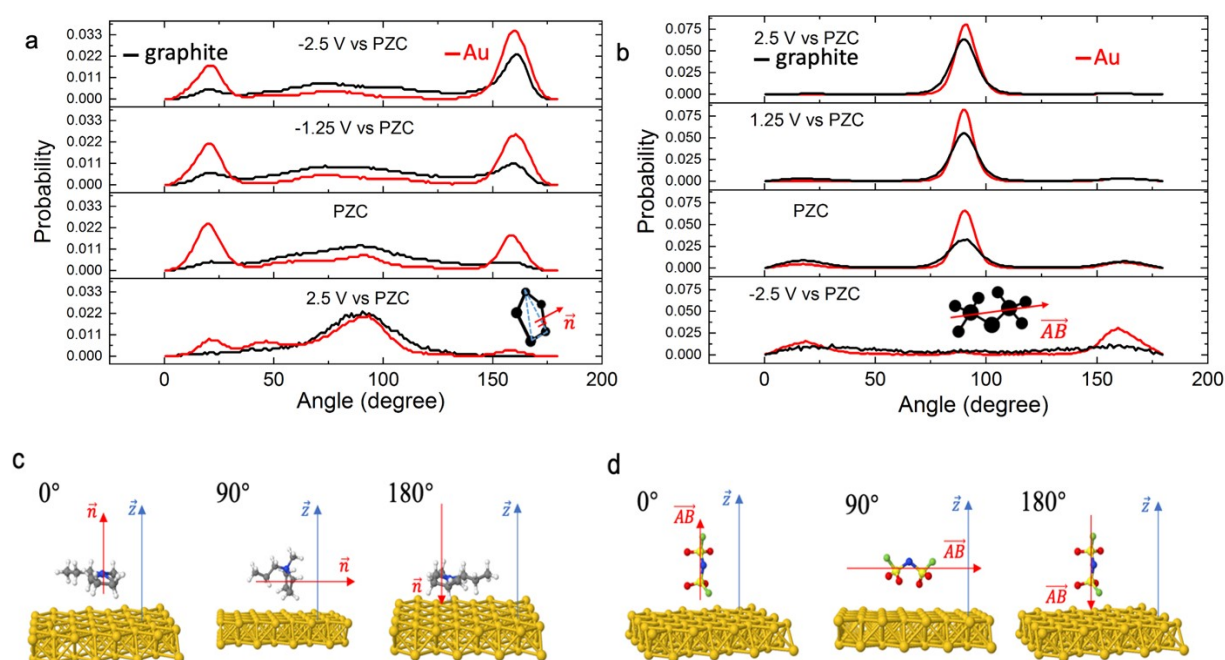
Email: dmitrii.rakov@research.deakin.edu.au; maria.forsyth@deakin.edu.au;

fangfang.chen@deakin.edu.au

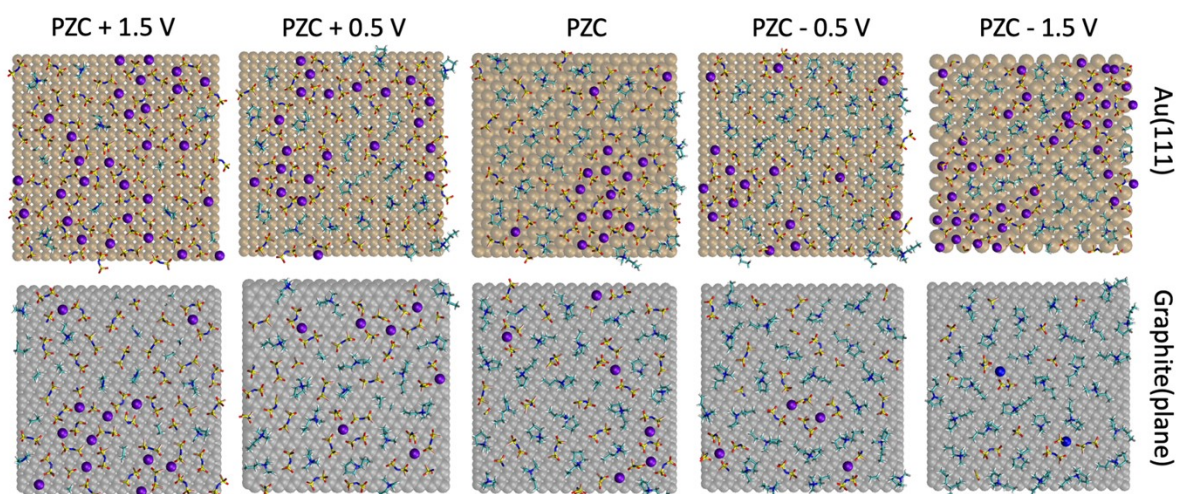


Supplementary Fig. 1 | 2D (x, y) snapshots of the innermost layer of C3mpyrFSI IL within 0.60 nm of the Au(111) and graphite (plane) surface. The snapshots were taken at a

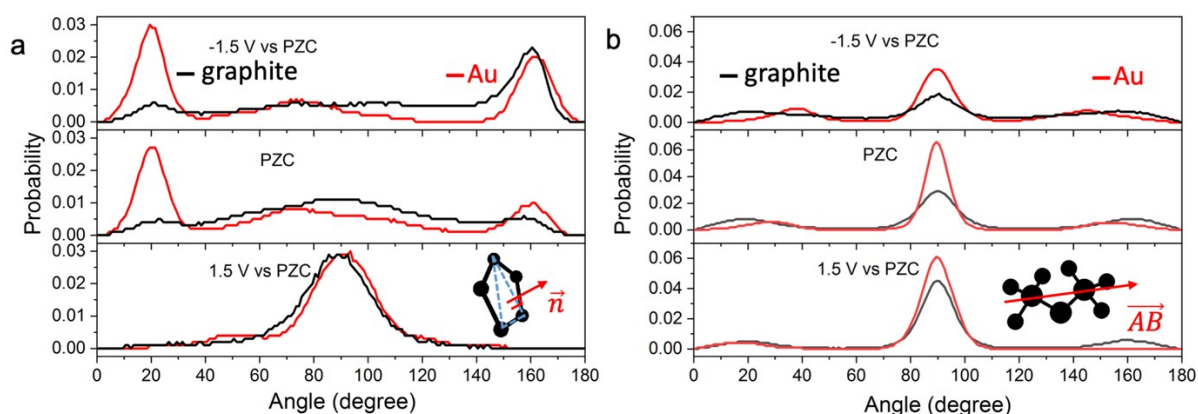
different applied potential. The uniform constant charge method (CCM) was applied to control electrostatic potential vs PZC.



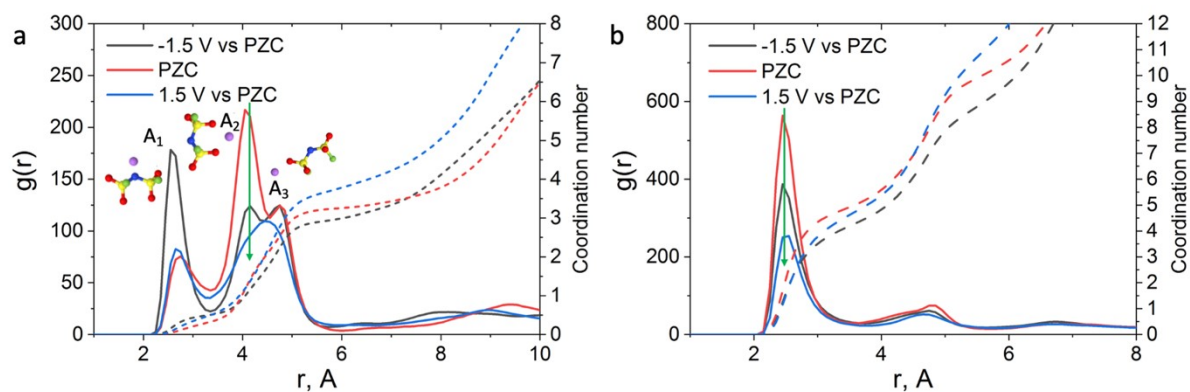
Supplementary Fig. 2 | Angular distribution analysis of (a) [C3mpyr]⁺ and (b) [FSI]⁻ in the innermost layer of IL next to the Au(111) and graphite (plane) surfaces. Angle orientation distribution of cations is analysed for the selected vector (\vec{n}) relative to the z axis (z axis is vertical to the electrode surface). Inset: Representation of the selected normal vector (\vec{n}) which is vertical to the pyrrolidinium ring. The peaks close to 90° or 0° / 180° stands for the orientation of [C3mpyr]⁺ ring which is either perpendicular or parallel to the electrode surface, respectively. Angle orientation distribution of anions analysed through vector (\vec{AB}) which is along of S-N-S bridge of [FSI]⁻. Its orientation is relative to the z axis (z axis is vertical to the electrode surface) is analysed. The peaks close to 90° or 0° / 180° stands for the S-N-S bridge of [FSI]⁻ which is either parallel or perpendicular to the electrode surface, respectively. The visual representation of (c) [C3mpyr]⁺ and (d) [FSI]⁻ orientation near the electrode surface. The uniform constant charge method (CCM) was applied to control electrostatic potential vs PZC.



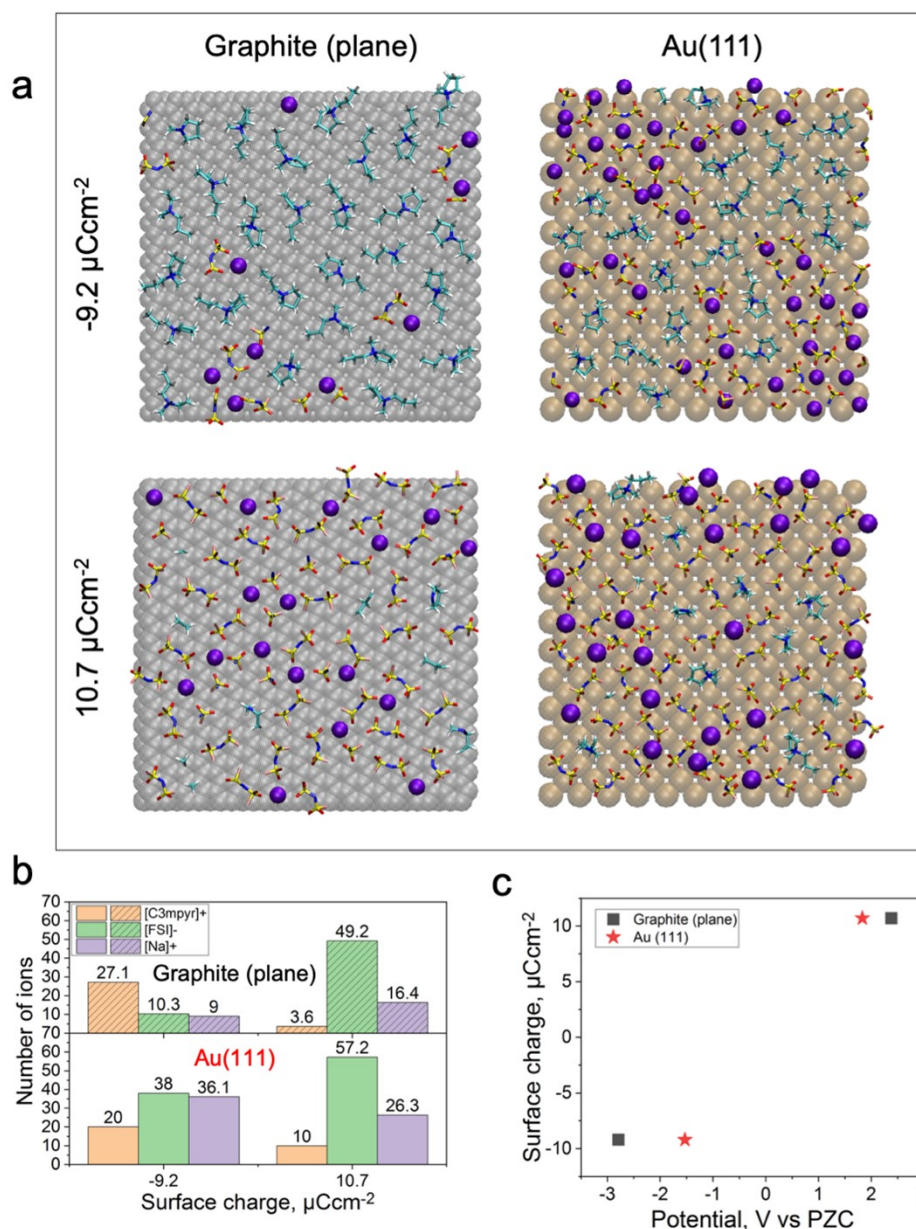
Supplementary Fig. 3 | 2D (x, y) snapshots of the innermost layer of C3mpyrFSI IL with 50 mol% NaFSI within 0.60 nm of the Au(111) and graphite (plane) surface. The snapshots were taken at a different applied potential. The uniform constant charge method (CCM) was applied to control electrostatic potential vs PZC.



Supplementary Fig. 4 | Angular distribution analysis of (a) [C3mpyr]⁺ and (b) [FSI]⁻ in the innermost layer of the superconcentrated IL next to the Au(111) and graphite (plane) surfaces. Angle orientation distribution of cations is analysed for the selected vector (\vec{n}) relative to the z axis (z axis is vertical to the electrode surface). Inset: Representation of the selected normal vector (\vec{n}) which is vertical to the pyrrolidinium ring. The peaks close to 90° or 0° / 180° stands for the orientation of [C3mpyr]⁺ ring which is either perpendicular or parallel to the electrode surface, respectively. Angle orientation distribution of anions analysed through vector (\vec{AB}) which is along of S-N-S bridge of [FSI]⁻. Its orientation is relative to the z axis (z axis is vertical to the electrode surface) is analysed. The peaks close to 90° or 0° / 180° stands for the S-N-S bridge of [FSI]⁻ which is either parallel or perpendicular to the electrode surface, respectively. The uniform constant charge method (CCM) was applied to control electrostatic potential vs PZC.



Supplementary Fig. 5 | Na-FSI coordination analysis through radial distribution function (RDF), $g(r)$, for 50 mol% NaFSI in C3mpyrFSI near the metallic gold electrode. (a) RDF and coordination number (CN) of Li-N_{FSI} coordination were calculated in the innermost layer within 0.6 nm from the Au(111) surface. (b) The RDF and CN of Li-O_{FSI} calculated in the innermost layer within 0.6 nm from the Au(111) surface. The uniform constant charge method (CCM) was applied to control electrostatic potential vs PZC.



Supplementary Fig. 6 | (a) 2D (x, y) snapshots of the innermost layer of C3mpyrFSI IL with 50 mol% NaFSI within 0.60 nm of the Au(111) and graphite (plane) surface. The snapshots were taken at a different applied surface charge. (b) Number of different ions in the innermost interfacial layer (within 0.6 nm the surface) for C3mpyrFSI with 50 mol% NaFSI at a different surface charge. (c) Surface charge vs potential plot for C3mpyrFSI IL with 50 mol% NaFSI with the Au(111) and graphite (plane) electrodes

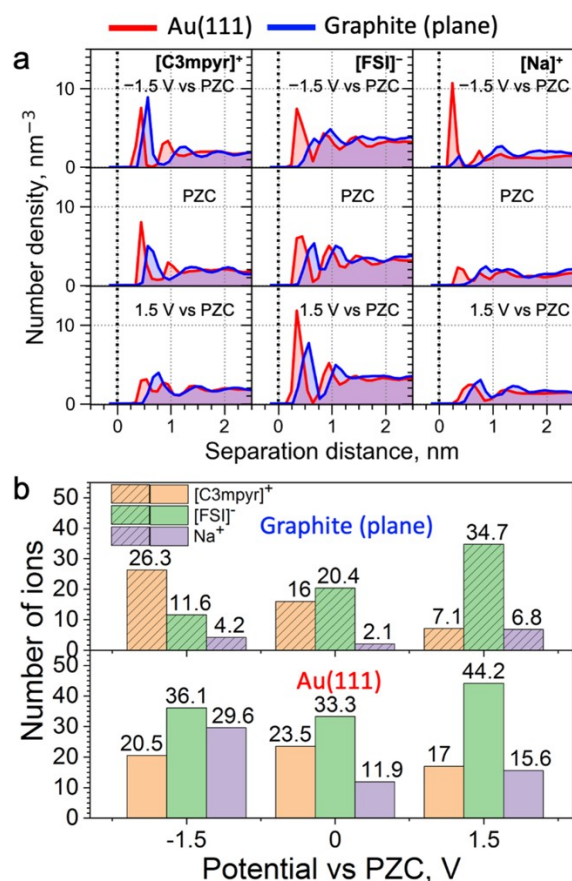
Supplementary Note 1. Molecular dynamic simulation of 50 mol% NaFSI in C3mpyrFSI near metallic and semiconductive electrode with a constant potential method.

Methods

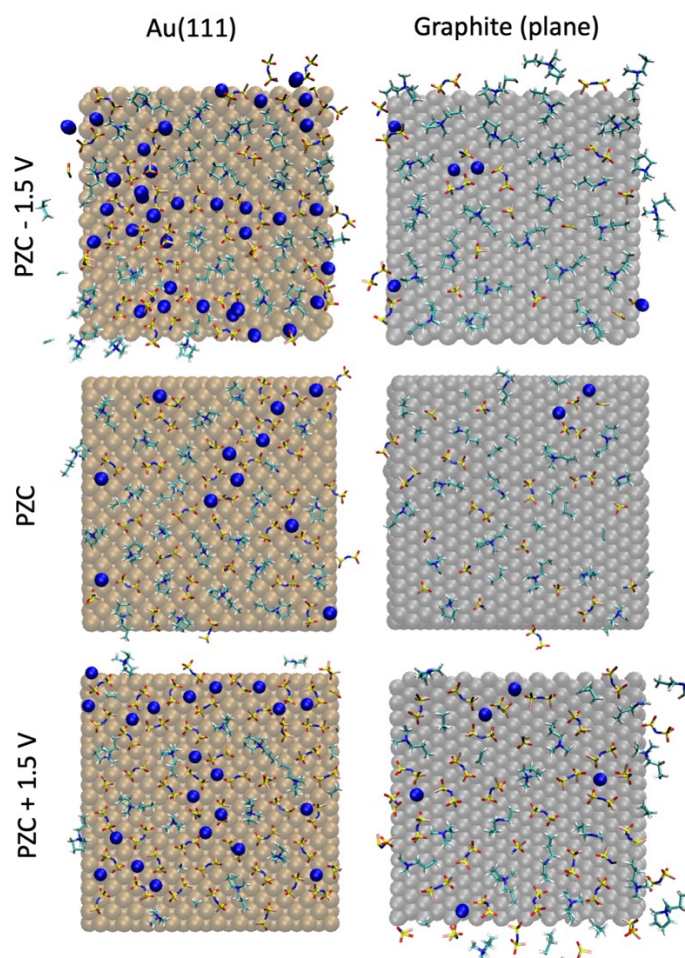
To estimate the effect of surface polarizability on the accuracy of our MD results with respect to Au(111) and graphite (plane) systems, we conducted constant potential method (CPM) MD simulations. All classical molecular dynamic simulation were conducted using an open-access LAMMPS simulation software package.¹ The Canongia Lopes-Padua (CL&P) non-polarizable force field was used in this work for Na⁺ and C3mpyrFSI ionic liquid.² The total ion net charge of all cations and anions was scaled down to ± 0.7 to account for ion-ion and ion-dipole interactions.² The Lennard-Jones potential parameters ($\epsilon=22.1333$ kJ/mol and $\sigma=0.2629$ nm) for face-centred cubic Au (111) electrode and ($\epsilon= 0.23059$ kJ/mol and $\sigma= 0.3412$ nm) for in plane translated hexagonal graphite electrode were adopted from literature.^{3,4} The simulation cell composition and dimensionally of Au(111)| 50 mol% NaFSI in C3mpyrFSI|Au(111) and graphite (plane)| 50 mol% NaFSI in C3mpyrFSI|graphite(plane) were adopted from those of the constant charge method (CCM) MD simulation with Gromacs software package.⁵ The electrodes were fixed during simulations. A cut-off radius for the Lennard-Jones and Coulombic interactions of 12 Å was used. An NVT annealing process was simulated at first by changing the temperature from 393 K to 700 K for 0.2 ns and kept at 700 K for 2 ns, and then the system was cooled back to 393 K within additional 0.5 ns. The annealing process allows the system to gain sufficient dynamics to obtain a reasonable initial structure for equilibration calculation. Both energies and pressures were checked to determine whether the system reaches the equilibrium. The additional 2.0 ns at 393 K was used for the NVT production run. The Nose-Hoover thermostat with a time constant of 100 fs was used for temperature coupling. A constant potential method (CPM) developed by Reed et al was used to control electrostatic potential between top layers of two electrodes.⁶ This method keeps constant potential by allowing atomic charges of the electrode to fluctuate (polarizable electrode surface) depending on the neighbouring environment, which is described as a Gaussian function. The Gaussian function parameter of 19.79 nm⁻¹ was used. The charges of electrolytes were kept fixed. The CPM was conducted with the *comp* module implemented in LAMMPS.⁷ The 3D-periodic Ewald summation with PPPM method was used to evaluate Coulombic interactions in the slab geometry. The trajectory was written with velocity Verlet algorithm every 1 ps. The data analysis was performed with customized Python script.⁸

Results and Discussion

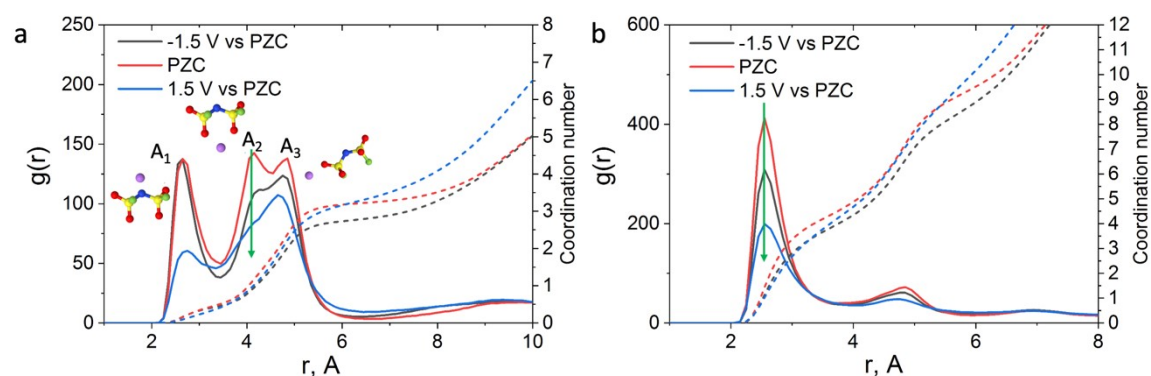
In general, it was found that the implementation of the CPM method does not alternate the conclusion described with an applied potential through the uniform constant charge MD method here as demonstrated in Fig. 1 (main text) and Supplementary Fig. 1-5 shown below. The CPM allows electrode surface polarizability which might affect the energy barrier for certain ions to reach the surface.⁷ In this regard, we decided to estimate the role of electrode material on the interfacial structure of 50 mol% NaFSI in C3mpyrFSI by using CPM MD simulations. As shown in Supplementary Fig. 7-8, the negative Au(111) electrode charging significantly increases the concentration of Na⁺ and [FSI]⁻ near the surface and decreases the number of [C3mpyr]⁺. In contrast, the graphite (plane) electrode at these conditions mostly increases the number of [C3mpyr]⁺ to screen the surface within the innermost layer and the number of [FSI]⁻ decreases almost twice compared to the system at PZC. The changes in the interfacial Na⁺ concentration are still minor and within an error compared to that of PZC conditions for both CPM and CCM MD simulations. When a positive potential is applied by using CPM methods the graphite surface still accumulates fewer Na⁺ in the form of Na_xFSI_y to screen the positive charge of the electrode compared to that of Au(111). The number of density analysis (Supplementary Fig. 7) also shows closer ion packing in the case of Au(111) surface compared to graphite (plane). The Na-FSI potential-driven coordination changes for Au(111) system within the innermost layer was estimated by RDF analysis (Supplementary Fig. 9). The CPM method shows similar Na⁺ coordination changes to those found with an applied potential through the CCM case (Supplementary Fig. 5 and Supplementary 9). Based on discussed results, it is fair to conclude that the impact of surface dielectric nature on the interfacial changes of superconcentrated ILs has the same trend for both CPM and CCM MD methods.



Supplementary Fig. 7 | Interfacial analysis of ionic liquids near Au (111) and graphite (plane) through CPM MD simulations (a–b). (a) Ion number density profiles of [C3mpyr]⁺, [FSI]⁻, and Na⁺ for C3mpyrFSI with 50 mol% NaFSI with (red) Au (111) and (blue) graphite (plane) electrodes at different applied potential vs PZC. Dash line represents the position of electrode surface. (b) Number of different ions in the innermost interfacial layer (within 0.6 nm the surface) for C3mpyrFSI with 50 mol% NaFSI at different potential vs PZC. The PZC stands for uncharged electrode conditions.

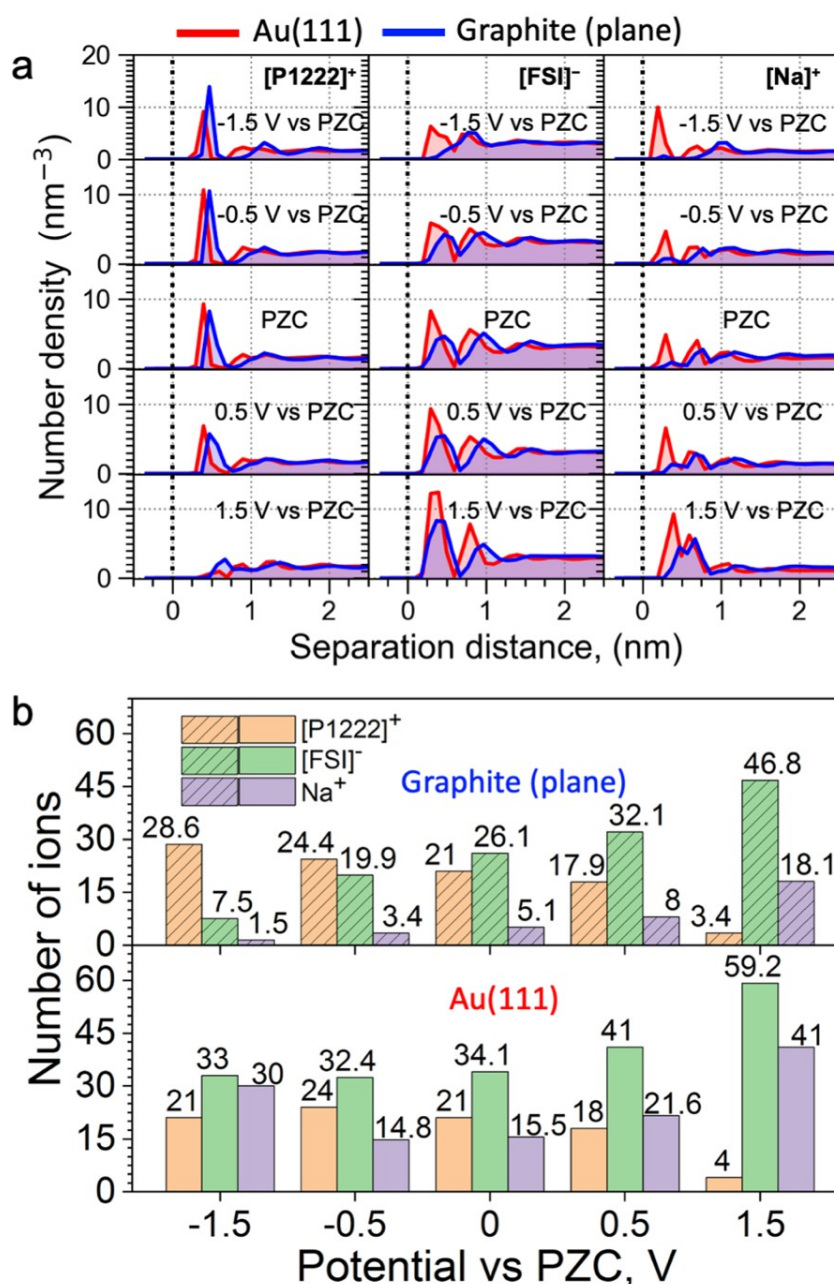


Supplementary Fig. 8 | 2D (x, y) snapshots of the innermost layer of C3mpyrFSI IL with 50 mol% NaFSI within 0.60 nm of the Au(111) and graphite (plane) surface by using CPM MD simulation. The snapshots were taken at different applied potentials under CPM conditions.

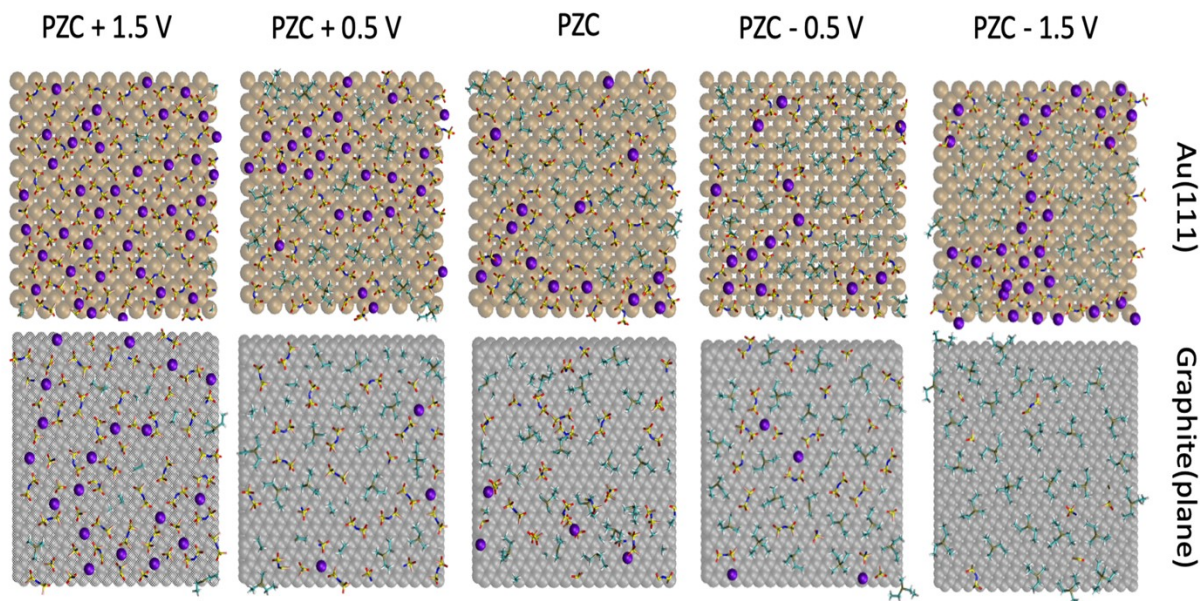


Supplementary Fig. 9 | Na-FSI coordination analysis of 50 mol% NaFSI in C3mpyrFSI near metallic gold electrode obtained through the constant potential method. (a) Radial distribution function (RDF), $g(r)$, and coordination number (CN) of Li-N_{FSI} calculated in the innermost layer within 0.6 nm from the Au(111) surface with 50 mol% NaFSI in C3mpyrFSI.

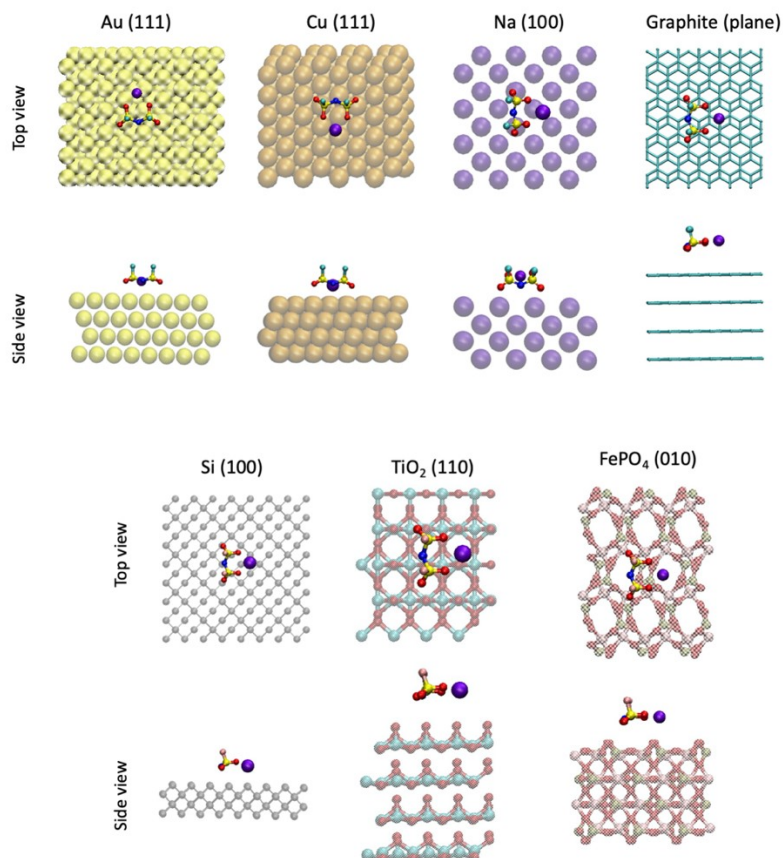
(b) The RDF and CN analysis of Li-O_{FSI} calculated in the innermost layer within 0.6 nm from the Au(111) surface with 50 mol% NaFSI in C3mpyrFSI. The CPM method was applied to control electrostatic potential vs PZC.



Supplementary Fig. 10 | Interfacial analysis of triethyl(methyl)phosphonium-based ionic liquids with Au (111) and graphite (plane) through the CCM MD simulations (a–b). (a) Ion number density profiles of [P1222]⁺, [FSI]⁻, and Na⁺ for P1222FSI with 50 mol% NaFSI with (red) Au (111) and (blue) graphite (plane) electrodes at different applied potential vs PZC. Dash line represents the position of electrode surface. (b) Number of different ions in the innermost interfacial layer (within 0.6 nm the surface) for P1222FSI with 50 mol% NaFSI at different potential vs PZC. The PZC stands for uncharged electrode conditions.



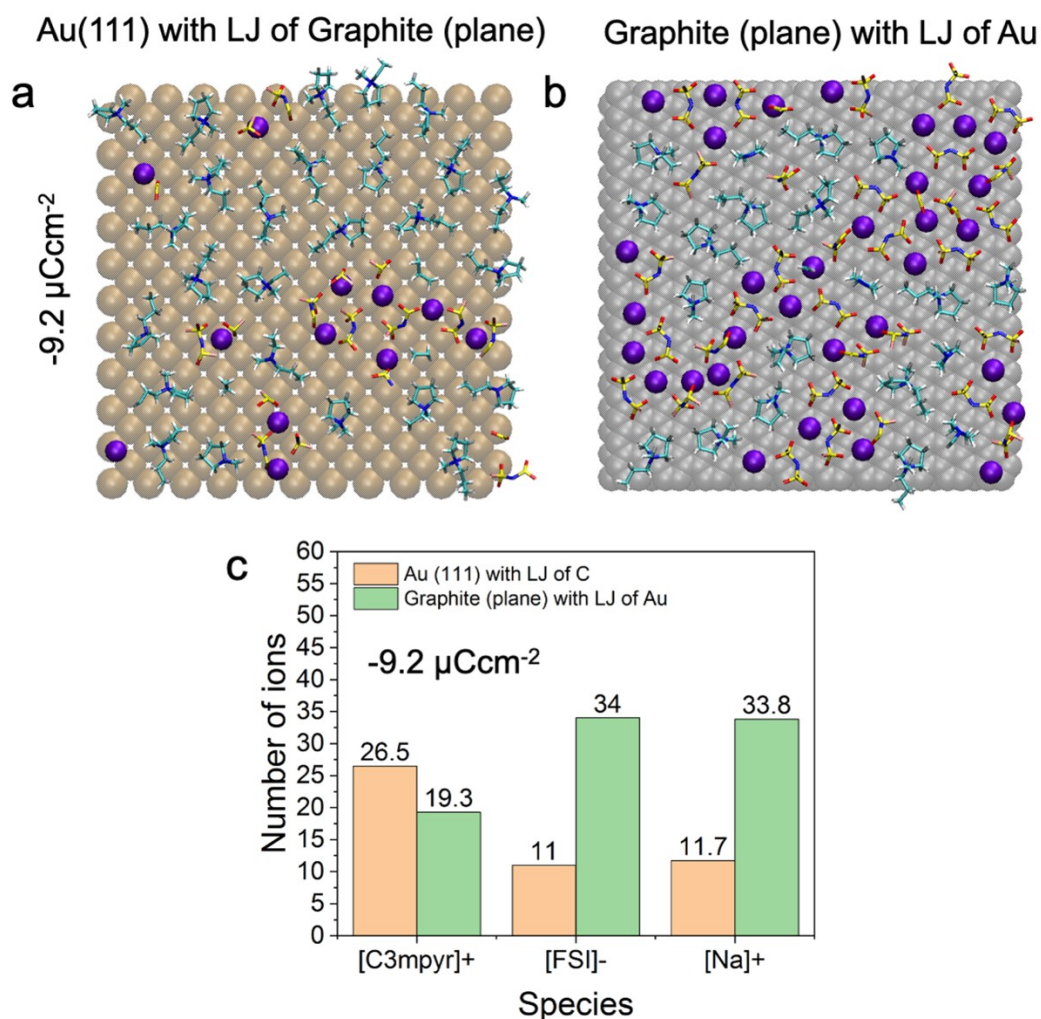
Supplementary Fig. 11 | 2D (x, y) snapshots of the innermost layer of P1222FSI IL with 50 mol% NaFSI within 0.60 nm of the Au(111) and graphite (plane) surface with triethyl(methyl)phosphonium-based ionic liquids. The snapshots were taken at a different applied potential. The CCM method was applied to control electrostatic potential vs PZC.



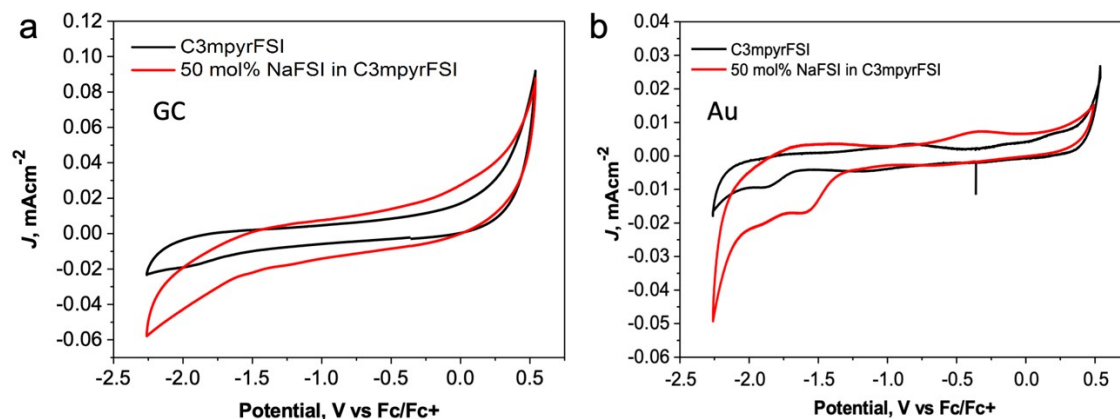
Supplementary Fig. 12 | Visual representation of pbc-DFT cells for NaFSI on the slab of different electrode material. The adsorption energy (E_{ad}) of NaFSI on different surfaces is presented in Fig 1e (main text).

Supplementary Table 1. Lennard-Jones parameters for different electrode materials adopted from literature

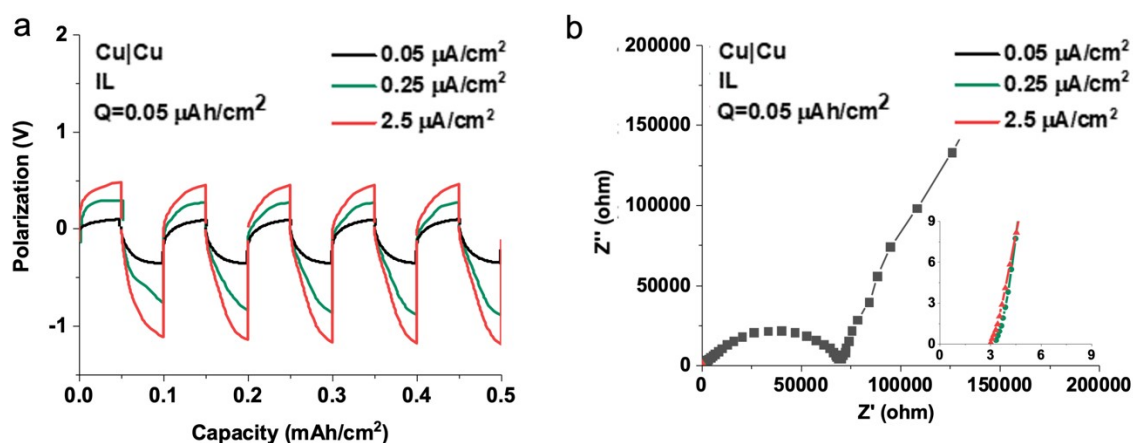
Element	R_0 , nm	Epsilon, kJ/mol	References
Au	0.2629	22.1333	Ref ⁹
Li	0.2800	9.0000	Ref ¹⁰
Cu	0.2616	19.748	Ref ¹¹
Si	0.2200	2.5104 (1.3388)	Ref ¹²
C (graphite)	0.3412	0.23059	Ref ¹³
TiO ₂	0.392 (Ti) 0.303 (O)	0.17154 (Ti) 0.50208 (O)	Ref ¹⁴



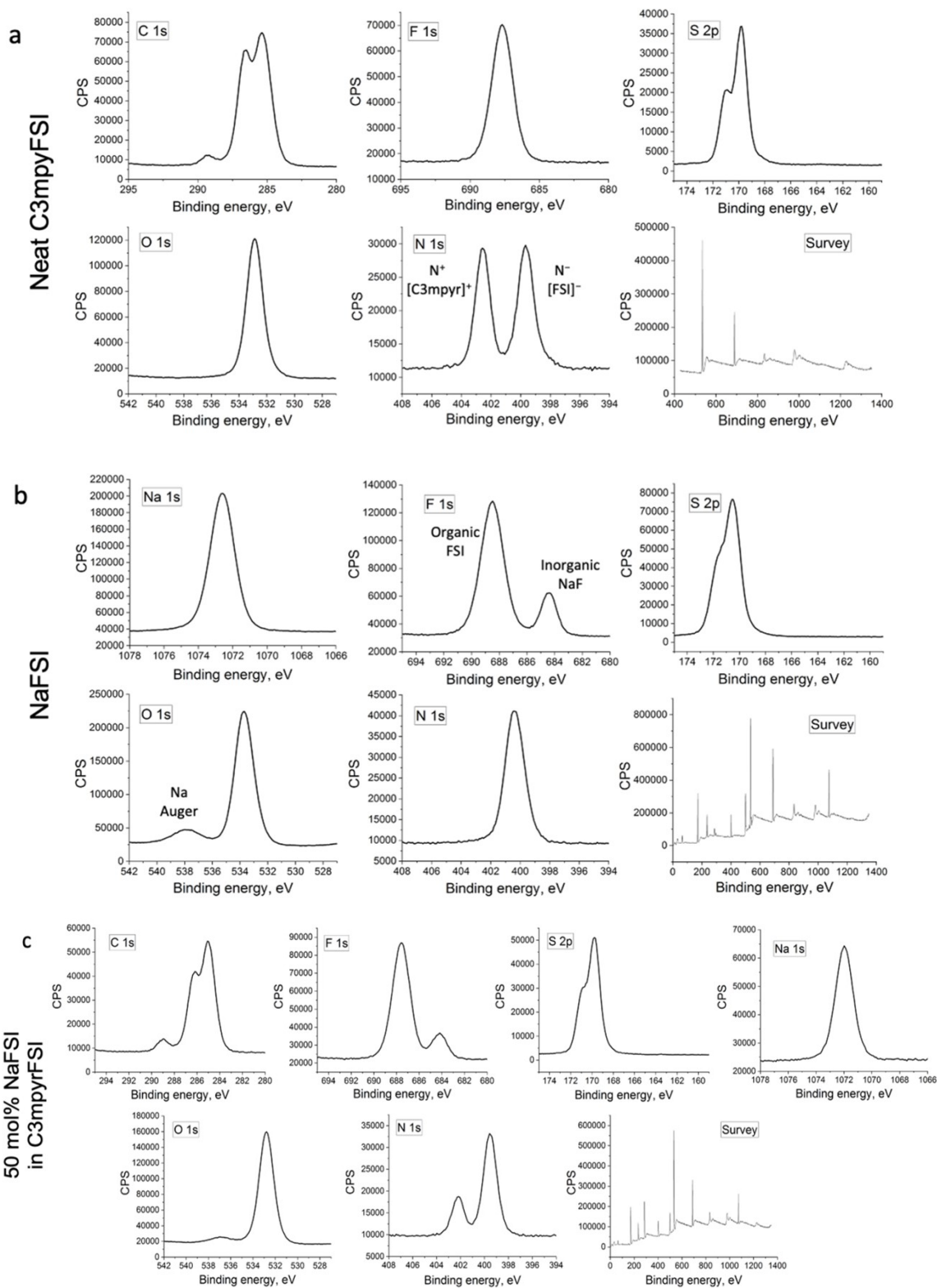
Supplementary Fig. 13 | The CCM MD simulation results for 50 mol% NaFSI in C3mpyrFSI near Au and graphite(plane) electrodes with swapped LJ parameters. 2D (x, y) snapshots of the innermost layer of C3mpyrFSI IL with 50 mol% NaFSI within 0.60 nm of the (a) Au(111) electrode with LJ of C and (b) graphite (plane) electrode with LJ of Au at $-9.2 \mu\text{Ccm}^{-2}$. (c) Number of different ions in the innermost interfacial layer (within 0.6 nm the surface) for C3mpyrFSI with 50 mol% NaFSI at at $-9.2 \mu\text{Ccm}^{-2}$.



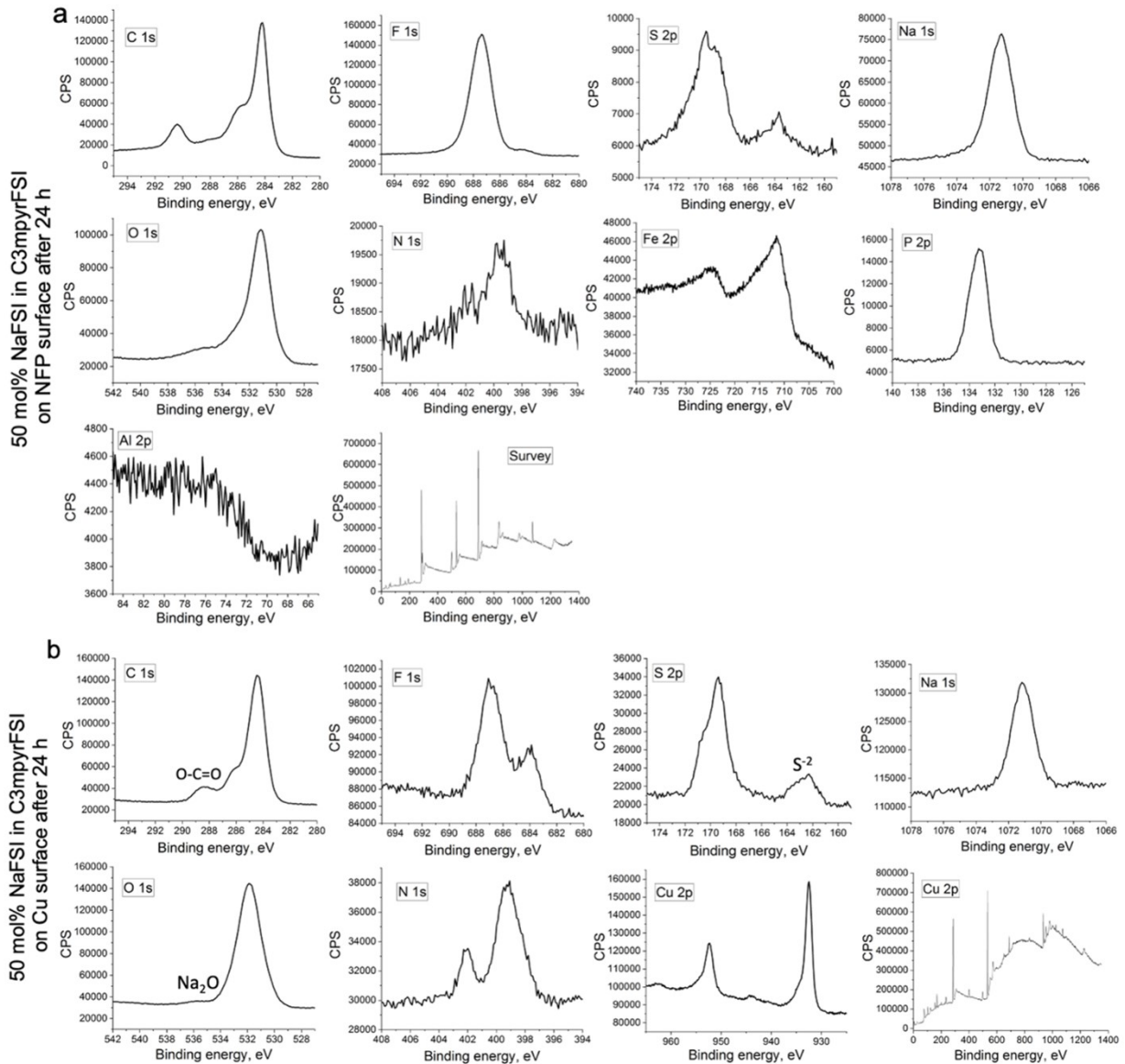
Supplementary Fig. 14 | Cycling voltammetry (CV) on glassy carbon and gold working electrodes with neat and superconcentrated IL. The CV of the first scan taken for neat C3mpyrFSI ($C_{\text{water}} < 78.3$ ppm) and C3mpyrFSI with 50 mol% NaFSI ($C_{\text{water}} < 87.9$ ppm) with (a) glassy carbon (GC) and (b) gold (Au) electrodes. The CV were performed at 50 °C with a scan rate of $25 \text{ mV} \cdot \text{s}^{-1}$ under Ar atmosphere.



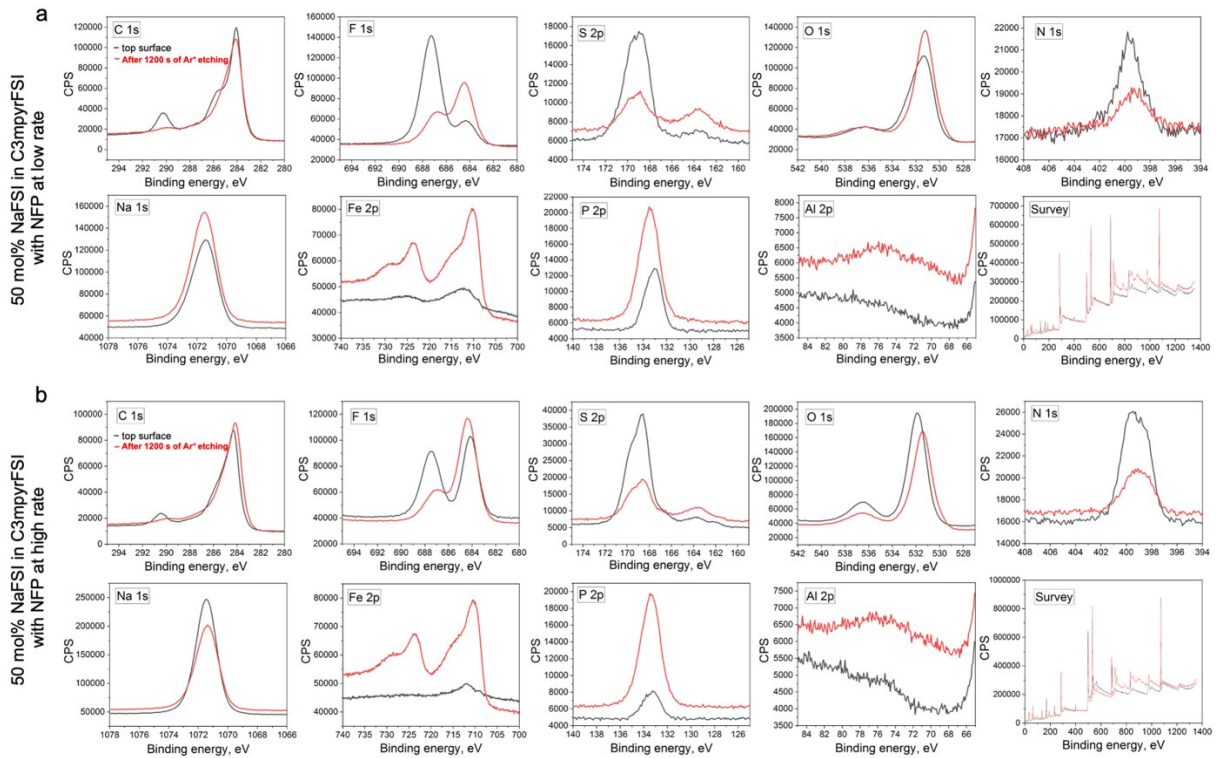
Supplementary Fig. 15 | Electrochemical data for Cu|50 mol% NaFSI in C3mpyrFSI|Cu cycling. (a) Cu symmetrical cells cycling with 50 mol% NaFSI in C3mpyrFSI at different rate and (b) EIS recorded after final cycle. The cycled cells were prepared for further XPS analysis of deposition products.



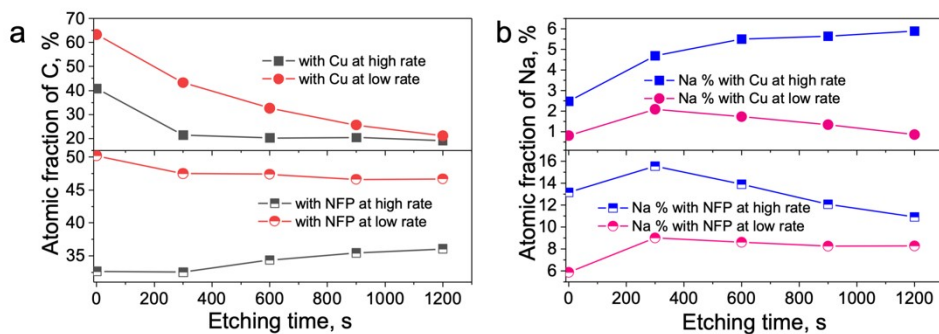
Supplementary Fig. 16 | High-resolution XPS spectrums for selected elements in examined electrolytes and sodium salt without an electrode material. XPS data for (a) neat C3mpyrFSI, (b) NaFSI, and (c) their NaFSI:C3mpyrFSI mixture (1:1 molar ratio).



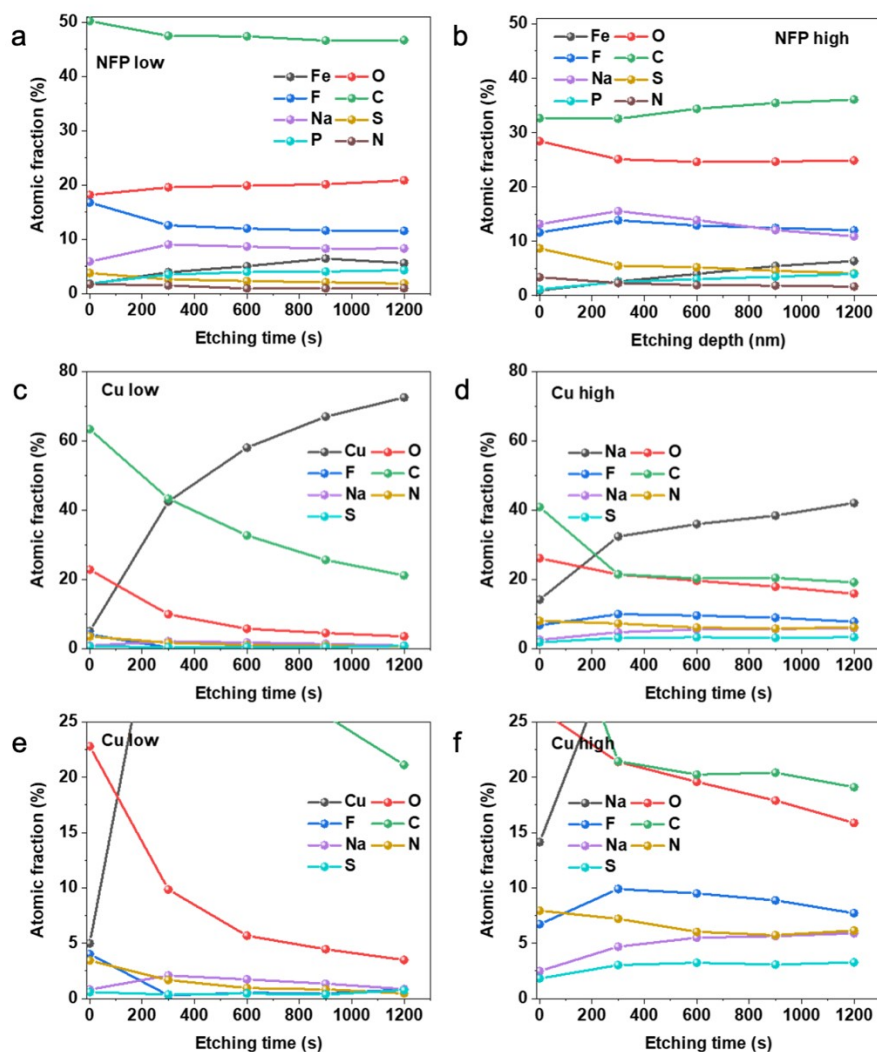
Supplementary Fig. 17 | High-resolution XPS spectra for selected elements of surface composition on NFP and Cu electrodes which were soaked in NaFSI:C3mpyrFSI mixture (1:1 molar ratio) for 24 h. XPS data for (a) NFP and (b) Cu electrodes.



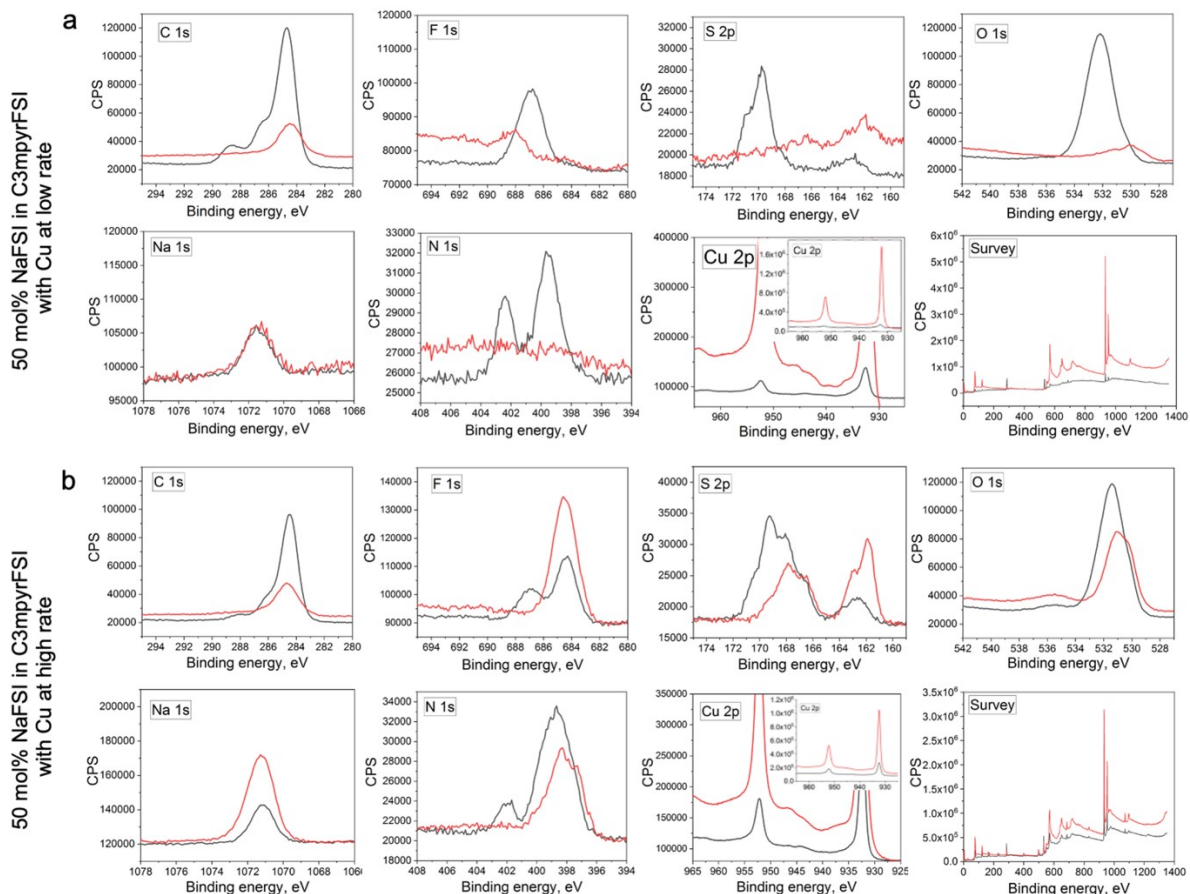
Supplementary Fig. 18 | High-resolution XPS spectra for selected elements of surface composition on NFP anodes after a final discharge cycle of preconditioning with NaFSI:C3mpyrFSI mixture (1:1 molar ratio) at low and high current density (fixed depth of charge). XPS data for (a) NFP preconditioned at low rate (low current density) of $0.05 \text{ mA}\cdot\text{cm}^{-2}/0.05 \text{ mAh}\cdot\text{cm}^{-2}$ and (b) NFP preconditioned at high rate (high current density) of $2.5 \text{ mA}\cdot\text{cm}^{-2}/0.05 \text{ mAh}\cdot\text{cm}^{-2}$. Top surface was analysed without Ar^+ etching (black line) which was applied to see a depth XPS profile after 1200 s of Ar^+ etching (red line).



Supplementary Fig. 19 | XPS elemental analysis with Ar^+ etching for (a) C % and (b) Na % in SEI of NFP and Cu anodes after their symmetrical cell preconditioning cycling with 50 mol% NaFSI in C3mpyrFSI at a different rate ($0.05 \text{ mA}\cdot\text{cm}^{-2}/0.05 \text{ mAh}\cdot\text{cm}^{-2}$ or $2.5 \text{ mA}\cdot\text{cm}^{-2}/0.05 \text{ mAh}\cdot\text{cm}^{-2}$ for NFP, and $0.05 \text{ }\mu\text{A}\cdot\text{cm}^{-2}/0.05 \text{ }\mu\text{Ah}\cdot\text{cm}^{-2}$ or $2.5 \text{ }\mu\text{A}\cdot\text{cm}^{-2}/0.05 \text{ }\mu\text{Ah}\cdot\text{cm}^{-2}$ for Cu).



Supplementary Fig. 20 | XPS elemental depth profile for deposition products on NFP and Cu anodes after a final discharge cycle of preconditioning with NaFSI:C3mpyrFSI mixture (1:1 molar ratio) at low and high current density (fixed depth of charge). XPS elemental depth profile for (a) NFP preconditioned at a low rate (low current density) of $0.05 \text{ mA}\cdot\text{cm}^{-2}/0.05 \text{ mAh}\cdot\text{cm}^{-2}$ and (b) NFP preconditioned at a high rate (high current density) of $2.5 \text{ mA}\cdot\text{cm}^{-2}/0.05 \text{ mAh}\cdot\text{cm}^{-2}$. XPS elemental depth profile for (c) Cu preconditioned at a low rate (low current density) of $0.05 \text{ }\mu\text{A}\cdot\text{cm}^{-2}/0.05 \text{ }\mu\text{Ah}\cdot\text{cm}^{-2}$ (with a magnified region in Supplementary Fig. 20e) and (d) Cu preconditioned at a high rate (high current density) of $2.5 \text{ }\mu\text{A}\cdot\text{cm}^{-2}/0.05 \text{ }\mu\text{Ah}\cdot\text{cm}^{-2}$ (with a magnified region in Supplementary Fig. 20f).



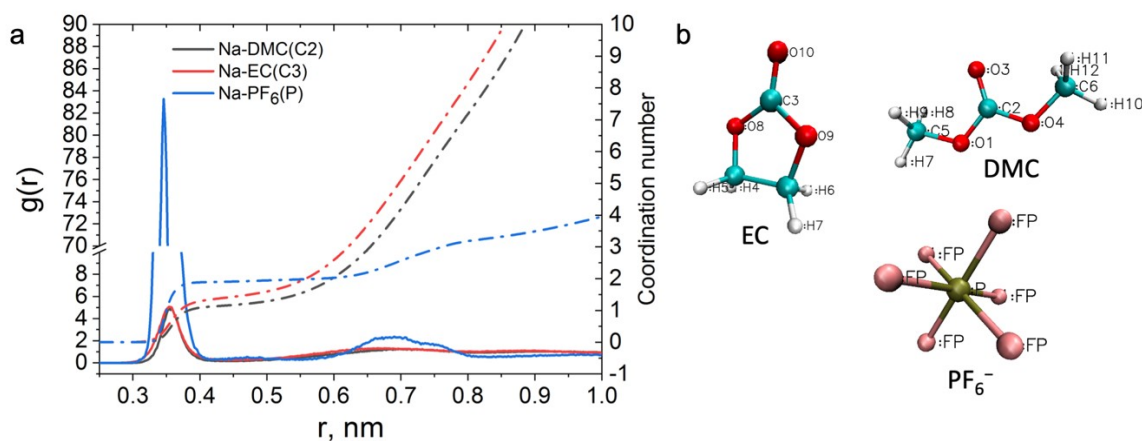
Supplementary Fig. 21 | High-resolution XPS spectrums for selected elements of surface composition on Cu anodes after a final discharge cycle of preconditioning with NaFSI:C3mpyrFSI mixture (1:1 molar ratio) at low and high current density (fixed depth of charge). XPS data for (a) Cu preconditioned at a low rate (low current density) of $0.05 \mu\text{A}\cdot\text{cm}^{-2}/0.05 \mu\text{Ah}\cdot\text{cm}^{-2}$ and (b) Cu preconditioned at a high rate (high current density) of $2.5 \mu\text{A}\cdot\text{cm}^{-2}/0.05 \mu\text{Ah}\cdot\text{cm}^{-2}$. Top surface was analysed without Ar^+ etching (black line) which was applied to see a depth XPS profile after 1200 s of Ar^+ etching (red line).

Supplementary Note 2. Molecular dynamic simulation of 1.0 M NaPF_6 in EC:DMC (1:1 by volume) near metallic and semiconductive electrode.

Methods

The molecular dynamic simulations were conducted with GROMACS software package.⁵ All electrolytes are equilibrated firstly at both 293, 312 and 393 K for more than 10s ns using the NPT ensemble and the Nose-Hoover and Parrinello-Rahman methods for temperature and pressure coupling. The densities were calculated through additional 7 ns MD trajectory. The pressure is set at 1 bar. The electrostatic interactions were computed using PME methods. An FTT grid spacing of 0.1 nm and cubic interpolation for charge distribution were used to

compute electrostatic interaction in reciprocal space. The cut-off distance of 1.2 nm was adopted for electrostatics and van der Waals interactions. The Velocity Verlet integrator was adopted with a time step of 1 fs. All studies were conducted based on classic all-atom molecular dynamic simulation with a non-polarizable force field. The force field parameters for NaPF₆ were taken from literature¹⁵¹⁶ without charge scaling. The EC and DMC parameters, including description of bonds, angles, and dihedrals were taken from previously reported work for LiPF₆ salt in EC:DMC (1:1) system.¹⁷ The atomic charges and description of non-bonded interactions for EC and DMC were adopted from other work.¹⁸ The charge scaling factor of 0.85 and 0.80 was used for EC and DMC molecules to optimize their mass density profile (Supplementary Table 2). The bulk phase of 1.0 M NaPF₆ in EC:DMC (1:1 by volume) was assembled by packing 31 ion pairs of NaPF₆ with 204 EC and 204 DMC molecules into cubic simulation box by means Packmol package.¹⁹ The calculated densities, listed in Table 6.1, show a good agreement with experimental results²⁰¹⁸, with only small error within $\pm 1.22\%$. The self-diffusion coefficients D of neat solvents were calculated at 298 K, and values of $1.51 \cdot 10^{-9} \text{ m}^2 \text{ s}^{-1}$ and $0.27 \cdot 10^{-9} \text{ m}^2 \text{ s}^{-1}$ for DMC and EC are very close to experimentally reported NMR results.²¹ The self-diffusion coefficients D of 1.0 M NaPF₆ in EC:DMC (1:1) were calculated at 293 K which are $0.412 \cdot 10^{-9} \text{ m}^2 \text{ s}^{-1}$, $0.298 \cdot 10^{-9} \text{ m}^2 \text{ s}^{-1}$, $0.034 \cdot 10^{-9} \text{ m}^2 \text{ s}^{-1}$, and $0.035 \cdot 10^{-9} \text{ m}^2 \text{ s}^{-1}$ for DMC, EC, PF₆⁻, and Na, respectively. Supplementary Fig. 22 shows the radial distribution (RDF) analysis for Na-ion solvation environment in 1.0 M NaPF₆ in EC:DMC (1:1) at 293 K, which is similar to the previously reported RDF profile of 1 M LiPF₆ in EC:DMC (1:1).²²¹⁷ Monti et al conducted Raman measurements for 1.0 M NaPF₆ in EC:DMC (1:1) to understand Na-ion solvation environment, and solvation number of EC and DMC was found to be 1.49 and 1.23 respectively.²⁰ The solvation number of the anion was not determined. As shown in Supplementary Fig. 22, the coordination number for the first Na-ion solvation shell at the distance of 0.405 nm equals to 1.31 (EC), 1.11 (DMC), and 1.90 (PF₆⁻) which further elucidates a good agreement between our MD results and experimental data.



S

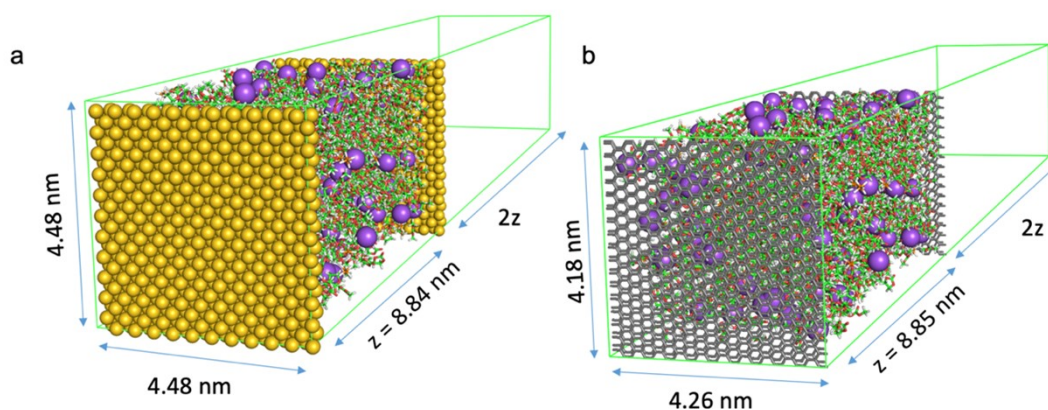
Supplementary Fig. 22 | Analysis of Na coordination analysis for 1.0 M NaPF₆ in EC:DMC (1:1) at 293 K. a) Radial distribution function (RDF), $g(r)$, and coordination number (CN) for Na-ion solvation shell calculated at 293 K in cin EC:DMC (1:1). b) Molecular representation for EC, DMC, and PF₆⁻ anion with atomic labelling used for the MD calculations.

Supplementary Table 2. Simulation and experimental physical-chemical properties of 1.0 M NaPF₆ EC:DMC (1:1) at different temperature. Simulated mass density (g/cm³) and box volume for neat EC, DMC and their 1.0 M NaPF₆ EC:DMC (1:1) mixture at 298 and 393 K. The experimental results²⁰¹⁸ are given in brackets (*experimental value) and compared with simulation results. The error of density is given in $\Delta = (D_{MD} - D_{exp}) / D_{exp} \times 100\%$.

T, K	Density, g cm ⁻³								
	EC	Δ , %	Box volume, nm ³	DMC	Δ , %	Box volume, nm ³	1.0 M NaPF ₆ EC:DMC (1:1)	Δ , %	Box volume, nm ³
393	–	–	–	–	–	–	1.165	–	59.20
312	1.307 (1.321)*	-1.06	39.13	1.042	–	50.21	1.269	–	54.36
293	1.326	–	38.57	1.067 (1.069)*	-0.18	49.02	1.292 (1.308)*	-1.22	53.35

Later, based on the obtained bulk density at 393 K the electrolyte was confined between Au(111) electrodes and Graphite (plane) electrodes with fixed x and y dimensions to have a separation distance (z) of about 8.8 nm (Supplementary Fig. 23 and Supplementary Table 2). The extra vacuum space of doubled z was added after the second electrode to eliminate periodic

artefact images resulting from simulation in slab geometry.²³ Before the main production run, an annealing process was simulated by changing the temperature from 393 K to 700 K to 393 K again for a total of 15 ns using an NVT ensemble and the Nose–Hoover thermostat. The annealing procedure allows the system to gain sufficient dynamics to obtain a reasonable initial structure for further calculation. Both energies and pressures were checked to determine whether the system reaches equilibrium. An additional 30-ns production run was performed at 393 K for structural and dynamics analysis. The trajectory file was written every 2 ps. The electrode charging was applied through uniform distribution of elementary charges (constant charge method) in the top layer of Au(111) and Graphite (plane) electrodes to produce relevant electrostatic potential. The electrode potential was determined according to Poisson equation^{24,25} by calculating the electric double layer (EDL) potential drop between two electrodes $U_{EDL} = \psi_{electrode} - \psi_{bulk}$. The U_{EDL} for uncharged electrode is a potential zero charge (PZC). The electrode potential vs. PZC is defined as $U_{EDL} = \psi_{electrode} - \psi_{bulk} - PZC$. Supplementary Table 3 shows surface charge density applied on the top layer of Au(111) and Graphite (plane) needed to generate relevant electrostatic potential. Trajectories were analysed by MDAnalysis code whenever the respective tool was unavailable in GROMACS.⁸ Quantum calculation (QC) for dipole moment were carried out with the Gaussian (G09) package using density functional theory (DFT).²⁶ The geometrical structures and vibrational modes of all molecules were calculated at Møller-Plesset second order perturbation theory level (MP2) with a 6-311++G(d,p) basis set in a gas phase.



Supplementary Fig. 23 | MD setups for 1.0 M NaPF₆ in EC:DMC (1:1) with metallic and semiconductive electrodes. a) MD setup for 1.0 M NaPF₆ in EC:DMC (1:1) with Au(111) electrodes at 393 K. b) MD setup for 1.0 M NaPF₆ in EC:DMC (1:1) with graphite (plane) electrodes at 393 K.

Supplementary Table 3. Details of electrodes charging for 1.0 M NaPF₆ in EC:DMC (1:1) studies. Surface charge density (e/nm²) to electrostatic potential (V vs PZC) in MD setups calculated via Poisson equation for the electrostatic drop across the electric-double layer.

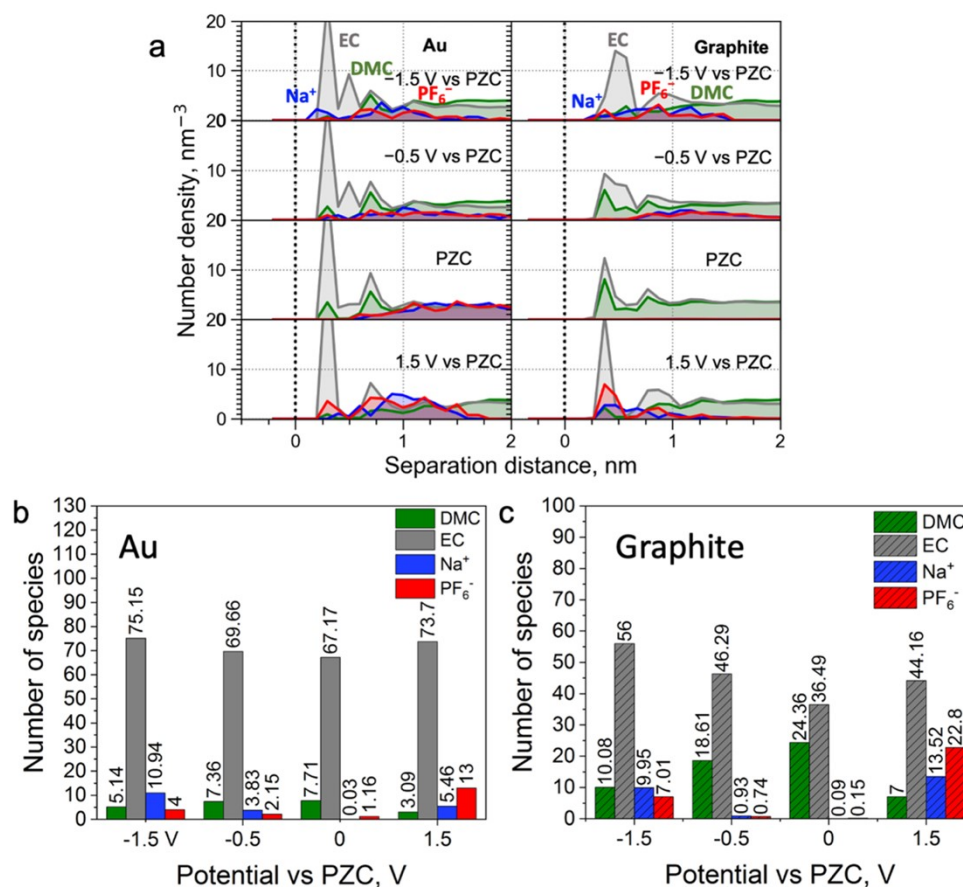
System	Au (111)	Graphite (plane)
Potential, V	Surface charge, e/nm ²	
-1.5 vs PZC	-0.55	-0.56
-0.5 vs PZC	-0.19	-0.16
PZC	0.00	0.00
1.5 vs PZC	0.43	0.51

Results and Discussion

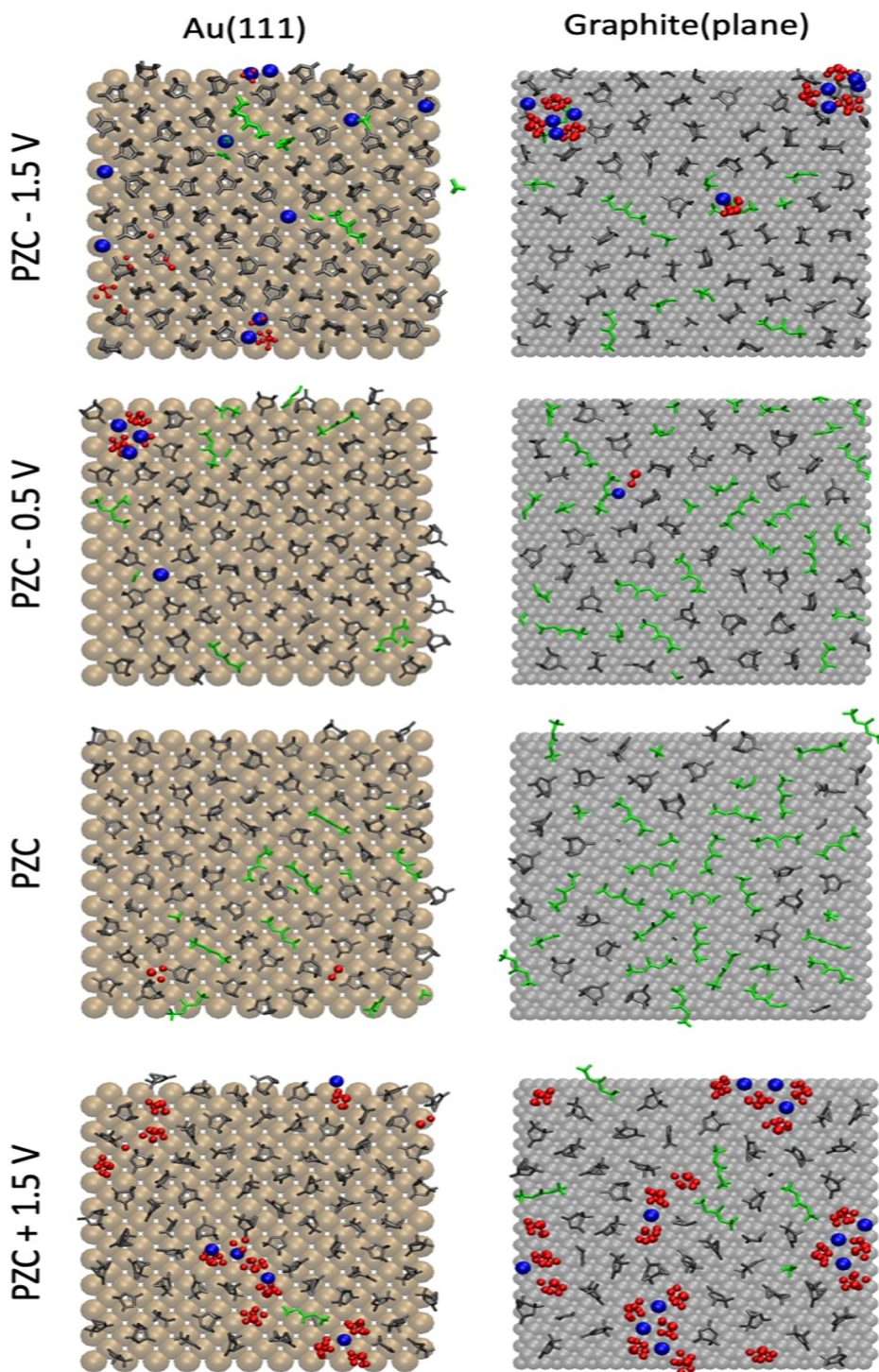
To estimate potential driven changes of commercial electrolyte within the electric-double layer near Au(111) and graphite (basal plane), the electrode/electrolyte interfaces of 1 M NaPF₆ in EC:DMC (1:1 v/v) were investigated by means of classical molecular dynamic simulations (MD) without modelling a decomposition process. Two different electrode configurations were modelled, namely, in Au(111)||Au(111) and graphite(basal plane)||graphite(basal plane) as shown Supplementary Fig. 23.

As shown in Supplementary Fig. 24a, commercial 1 M NaPF₆ in EC:DMC (1:1 v/v) demonstrates a typical interfacial layering profile of carbonate-based electrolyte which extends to within a nm from electrode surface to the bulk phase²⁷⁻²⁹. The focus is placed on the electrolyte layer next to the negative electrode surface here since its composition directly affects the initial stage of SEI formation. This electrolyte layer contains all ions and solvent species, but in different quantities that respond differently to the applied potential. In contrast to ILs, the commercial carbonate 1 M NaPF₆ electrolyte delivers salt component closer to both metallic Au(111) and semiconductive graphite (plane) electrode surfaces upon higher applied potential (Supplementary Fig. 24a and c, Supplementary Fig. 25). This is due to the absence of competing cationic species at the negative interface, e.g., IL cation, which explains the reason for favourable SEI/morphology formation upon higher negative surface polarization with both metallic and semiconductive electrodes^{30,31}. The high positive electrode potential also brings more salt competent in Na_xPF_{6y} (y > x) form to compensate surface charge, which

further elucidates the application of both negative and positive polarization (higher cell voltage) to form favourable, SEI, CEI, and deposition morphology.



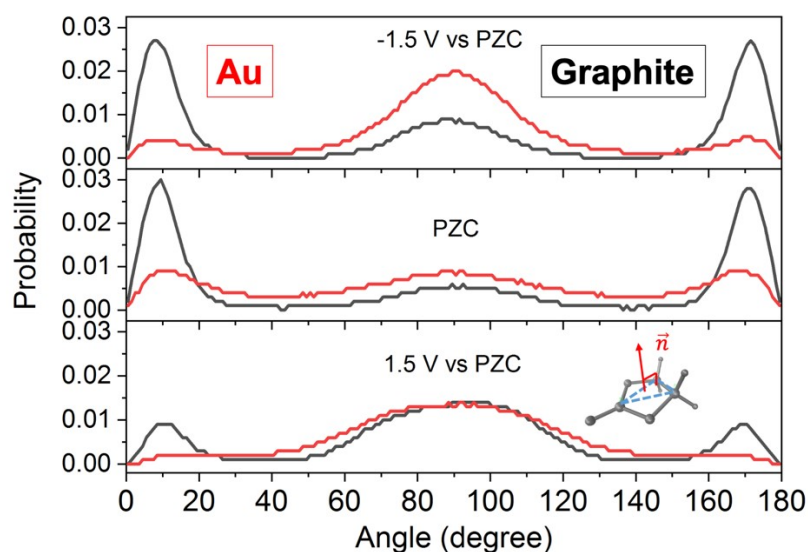
Supplementary Fig. 24 | Interface composition for 1.0 M NaPF₆ in EC:DMC (1:1) with metallic and semiconductive electrodes. a) Number density for the electrolyte species of 1.0 M NaPF₆ in EC:DMC (1:1) near Au(111) (right) and near graphite (plane) at different applied potential. Number of species of 1.0 M NaPF₆ in EC:DMC (1:1) within 0.6 nm from the b) Au(111) and c) graphite (plane) surface upon different polarization.



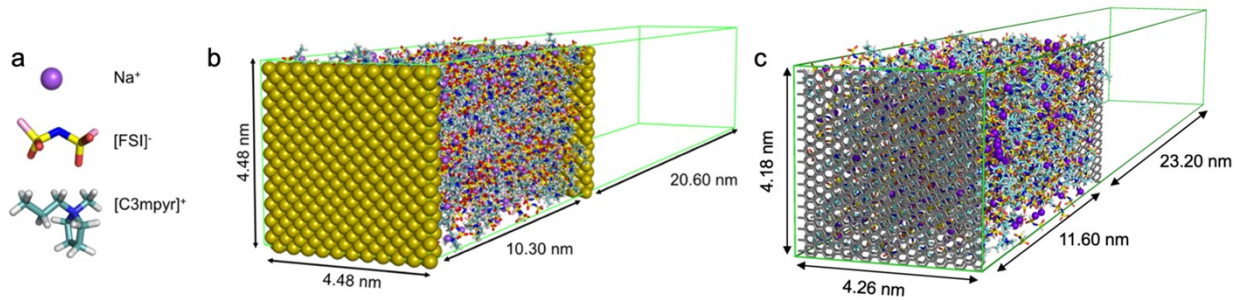
Supplementary Fig. 25 | Innermost layer composition for 1.0 M NaPF₆ in EC:DMC (1:1) with metallic and semiconductive electrodes. a) Snapshot of the innermost layer (0.6 nm from the surface) of 1.0 M NaPF₆ in EC:DMC (1:1) near Au(111) (right) and near graphite (plane) at different applied potential. The colour codes of species are as follows: DMC (green), EC (grey), Na⁺ (blue), PF₆⁻ (red).

Regarding solvent molecules, both negative and positive electrode charging brings more EC than DMC to the surface (Supplementary Fig. 24a and c, and Supplementary Fig. 25), and the same trend was observed for 1 M LiPF₆ in EC:DMC (1:1) with polarizable and non-polarizable force field^{28,29}. This can be explained due to different structure of solvent molecules, e.g., EC is more compact than DMC which results to higher dipole moment and polarization³² of EC (6.17 D and $\epsilon=90.03$) to that of DMC (0.23 D and $\epsilon=3.10$), therefore, EC responds to electric field more efficiently compared to DMC³². The dominance of EC at the interface explains the formation of alkoxy ROCO₂Na and carbonate Na₂CO₃ components over NaF.^{33–35}

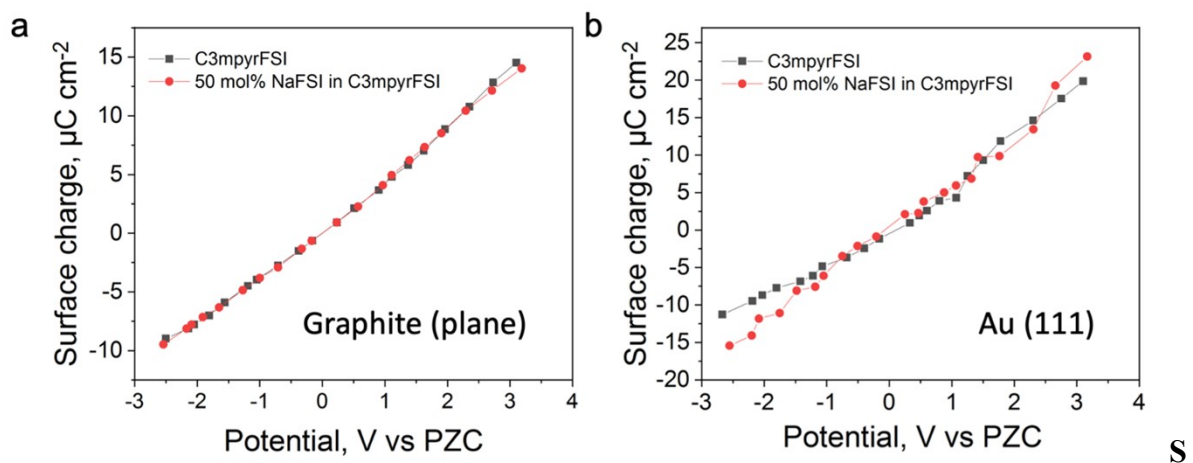
Similar to ILs, the metallic Au(111) demonstrates stronger van der Waals (VdW) interactions (closer position to the surface) with the whole electrolyte compared to that of graphite (plane) surface, which in particular results in significantly different EC orientation in the innermost layer (Supplementary Fig. 24-26). Specifically, the applying negative -1.5 V vs PZC potential forces EC ring to be parallel to Au(111) and perpendicular to the graphite (plane) surface. As for positive 1.5 V vs PZC potential, the EC ring is completely perpendicular to the graphite (plane) surface and mixed parallel/ perpendicular orientation was found near Au(111) surface. This can be explained by different VdW interactions with the surfaces, namely, Au(111) can keep both positive and negative sites of polar EC molecules due to strong dispersion forces. In contrast, semiconductive graphite (plane) electrode with weak VdW interactions is forced to realize selective EC orientation upon electrostatic adsorption. These findings may have a potential application for electrolyte engineering, where a response to the interface composition from electrostatic potential and near-surface molecular orientation can be tuned by varying an electrode surface and a solvent with certain dielectric properties.



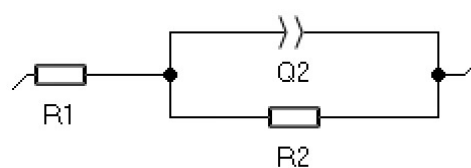
Supplementary Fig. 26 | Angular distribution analysis of EC in the inner most layer next to the Au(111) and graphite (plane) surface. Angle orientation distribution of vector (\vec{n}) relative to the z axis (z axis is vertical to the electrode surface). The peaks close to 90° and $0^\circ / 180^\circ$ stands for the EC ring perpendicular or parallel to the electrode surface, respectively. Inset: Representation of the selected normal vector (\vec{n}) which is vertical to the EC ring.



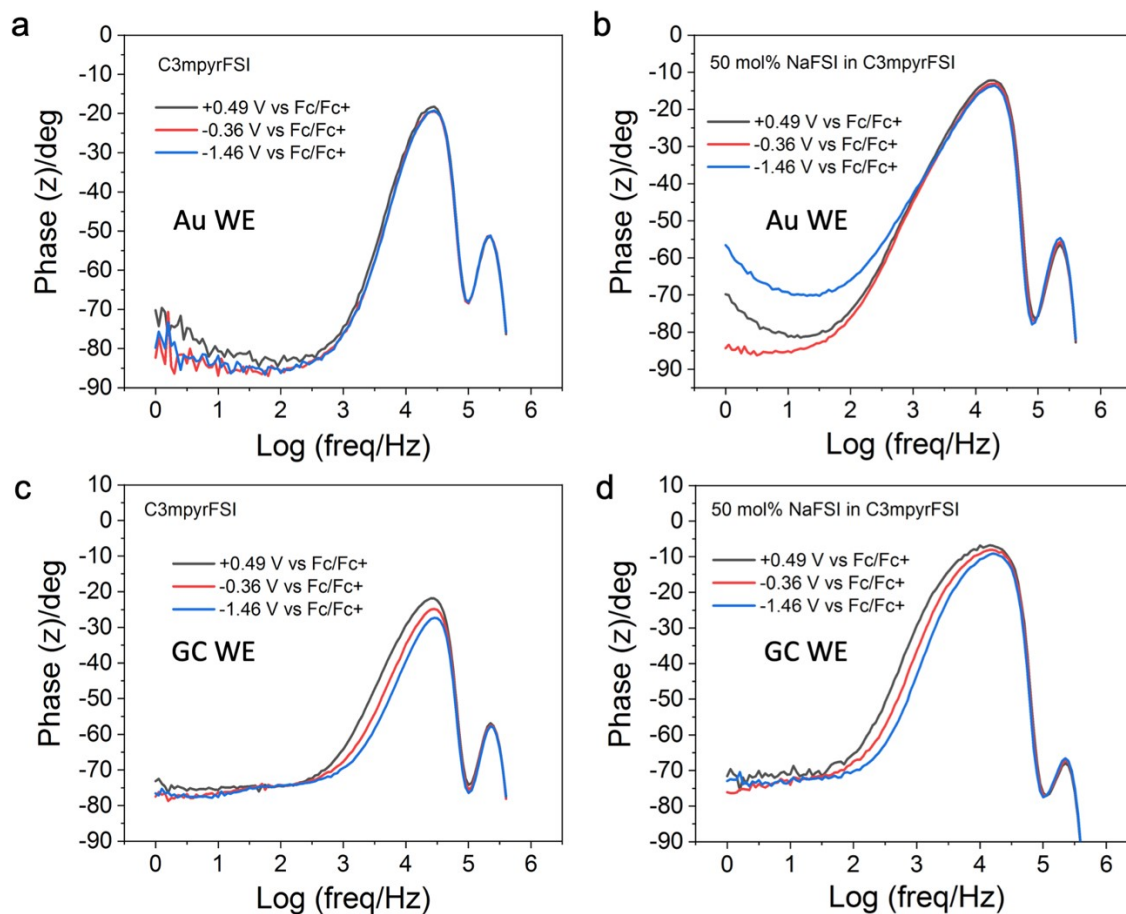
Supplementary Fig. 27 | MD setups for interfacial studies of neat C3mpyrFSI and 50 mol% NaFSI in C3mpyrFSI with metallic and semiconductive electrodes. a) Visual presentation of electrolyte constituents b) MD setup for 50 mol% NaFSI in C3mpyrFSI with Au(111) electrodes at 393 K. c) MD setup for 50 mol% NaFSI in C3mpyrFSI with Graphite (plane) electrodes at 393 K.



supplementary Fig. 28 | The relation between surface charge density (σ) and potential on the electrode for neat C3mpyrFSI and 50 mol% NaFSI in C3mpyrFSI with (a) semiconductive graphite (plane) and (b) metallic Au (111) electrodes.



Supplementary Fig. 29 | Circuit model for a differential capacitance study with electrolyte in three-electrodes setup.



Supplementary Fig. 30 | Phase angle vs log(freq) plot collected at different potentials for (a) neat C3mpyrFSI and (b) 50 mol% NaFSI in C3mpyrFSI with gold working electrode and for (c) neat C3mpyrFSI and (d) 50 mol% NaFSI in C3mpyrFSI with GC working electrode.

References

1. Plimpton, S. Fast parallel algorithms for short-range molecular dynamics. *J. Comput. Phys.* **117**, 1–19 (1995).
2. Chen, F., Howlett, P. & Forsyth, M. Na-Ion solvation and high transference number in superconcentrated ionic liquid electrolytes: a theoretical approach. *J. Phys. Chem. C* **122**, 105–114 (2018).
3. Wang, R., Bi, S., Presser, V. & Feng, G. Systematic comparison of force fields for molecular dynamic simulation of Au (111)/Ionic liquid interfaces. *Fluid Phase Equilib.* **463**, 106–113 (2018).

4. Hirunsit, P. & Balbuena, P. B. Effects of confinement on water structure and dynamics: a molecular simulation study. *J. Phys. Chem. C* **111**, 1709–1715 (2007).
5. Lindahl, E., Hess, B. & van der Spoel, D. GROMACS 3.0: a package for molecular simulation and trajectory analysis. *Mol. Model. Annu.* **7**, 306–317 (2001).
6. Reed, S. K., Lanning, O. J. & Madden, P. A. Electrochemical interface between an ionic liquid and a model metallic electrode. *J. Chem. Phys.* **126**, 84704 (2007).
7. Wang, Z., Yang, Y., Olmsted, D. L., Asta, M. & Laird, B. B. Evaluation of the constant potential method in simulating electric double-layer capacitors. *J. Chem. Phys.* **141**, 184102 (2014).
8. Michaud-Agrawal, N., Denning, E. J., Woolf, T. B. & Beckstein, O. MDAAnalysis: a toolkit for the analysis of molecular dynamics simulations. *J. Comput. Chem.* **32**, 2319–2327 (2011).
9. Wang, R., Bi, S., Presser, V. & Feng, G. Systematic comparison of force fields for molecular dynamic simulation of Au(111)/Ionic liquid interfaces. *Fluid Phase Equilib.* **463**, 106–113 (2018).
10. Ebadi, M., Costa, L. T., Araujo, C. M. & Brandell, D. Modelling the Polymer Electrolyte/Li-Metal Interface by Molecular Dynamics Simulations. *Electrochim. Acta* **234**, 43–51 (2017).
11. Heinz, H., Vaia, R. A., Farmer, B. L. & Naik, R. R. Accurate simulation of surfaces and interfaces of face-centered cubic metals using 12–6 and 9–6 Lennard-Jones potentials. *J. Phys. Chem. C* **112**, 17281–17290 (2008).
12. Sieffert, N. & Wipff, G. Ordering of imidazolium-based ionic liquids at the α -quartz (001) surface: a molecular dynamics study. *J. Phys. Chem. C* **112**, 19590–19603 (2008).
13. Hirunsit, P. & Balbuena, P. B. Effects of confinement on water structure and dynamics: A molecular simulation study. *J. Phys. Chem. C* **111**, 1709–1715 (2007).
14. Singh, R., Rajput, N. N., He, X., Monk, J. & Hung, F. R. Molecular dynamics simulations of the ionic liquid [EMIM⁺][TFMSI⁻] confined inside rutile (110) slit nanopores. *Phys. Chem. Chem. Phys.* **15**, 16090–16103 (2013).
15. Chen, F. & Forsyth, M. Elucidation of transport mechanism and enhanced alkali ion transference numbers in mixed alkali metal–organic ionic molten salts. *Phys. Chem. Chem. Phys.* **18**, 19336–19344 (2016).
16. Kaminski, G. A. & Jorgensen, W. L. Host–guest chemistry of rotaxanes and catenanes: application of a polarizable all-atom force field to cyclobis(paraquat-p-phenylene)

- complexes with disubstituted benzenes and biphenyls. *J. Chem. Soc. Perkin Trans. 2* 2365–2375 (1999).
17. Haghkhah, H., Choobar, B. G. & Amjad-Iranagh, S. Effect of salt concentration on properties of mixed carbonate-based electrolyte for Li-ion batteries: a molecular dynamics simulation study. *J. Mol. Model.* **26**, 1–15 (2020).
 18. Soetens, J.-C., Millot, C., Maigret, B. & Bakó, I. Molecular dynamics simulation and X-ray diffraction studies of ethylene carbonate, propylene carbonate and dimethyl carbonate in liquid phase. *J. Mol. Liq.* **92**, 201–216 (2001).
 19. Martínez, L., Andrade, R., Birgin, E. G. & Martínez, J. M. PACKMOL: A package for building initial configurations for molecular dynamics simulations. *J. Comput. Chem.* **30**, 2157–2164 (2009).
 20. Monti, D. *et al.* Towards standard electrolytes for sodium-ion batteries: physical properties, ion solvation and ion-pairing in alkyl carbonate solvents. *Phys. Chem. Chem. Phys.* **22**, 22768–22777 (2020).
 21. Hayamizu, K., Aihara, Y., Arai, S. & Martinez, C. G. Pulse-gradient spin-echo ^1H , ^7Li , and ^{19}F NMR diffusion and ionic conductivity measurements of 14 organic electrolytes containing $\text{LiN}(\text{SO}_2\text{CF}_3)_2$. *J. Phys. Chem. B* **103**, 519–524 (1999).
 22. Skarmoutsos, I., Ponnuchamy, V., Vetere, V. & Mossa, S. Li^+ solvation in pure, binary, and ternary mixtures of organic carbonate electrolytes. *J. Phys. Chem. C* **119**, 4502–4515 (2015).
 23. Fedorov, M. V. & Kornyshev, A. A. Ionic Liquids at Electrified Interfaces. *Chem. Rev.* **114**, 2978–3036 (2014).
 24. Velpula, G. *et al.* Graphene meets ionic liquids: fermi level engineering via electrostatic forces. *ACS Nano* **13**, 3512–3521 (2019).
 25. Vatamanu, J., Xing, L., Li, W. & Bedrov, D. Influence of temperature on the capacitance of ionic liquid electrolytes on charged surfaces. *Phys. Chem. Chem. Phys.* **16**, 5174–5182 (2014).
 26. Gaussian09, R. 01, Frisch MJ *et al.*, Gaussian. *Inc.*, Wallingford CT (2009).
 27. Xing, L., Vatamanu, J., Borodin, O., Smith, G. D. & Bedrov, D. Electrode/electrolyte interface in sulfolane-based electrolytes for Li ion batteries: a molecular dynamics simulation study. *J. Phys. Chem. C* **116**, 23871–23881 (2012).
 28. Vatamanu, J., Borodin, O. & Smith, G. D. Molecular dynamics simulation studies of the structure of a mixed carbonate/ LiPF_6 electrolyte near graphite surface as a function of electrode potential. *J. Phys. Chem. C* **116**, 1114–1121 (2012).

29. Boyer, M. J., Vilčiauskas, L. & Hwang, G. S. Structure and Li⁺ ion transport in a mixed carbonate/LiPF₆ electrolyte near graphite electrode surfaces: a molecular dynamics study. *Phys. Chem. Chem. Phys.* **18**, 27868–27876 (2016).
30. Aleshin, A., Bravo, S., Redquest, K. & Wood, K. N. Rapid Oxidation and Reduction of Lithium for Improved Cycling Performance and Increased Homogeneity. *ACS Appl. Mater. Interfaces* **13**, 2654–2661 (2021).
31. Kishore, B., Chen, L., Dancer, C. E. J. & Kendrick, E. Electrochemical formation protocols for maximising the life-time of a sodium ion battery. *Chem. Commun.* **56**, 12925–12928 (2020).
32. Daniels, I. N., Wang, Z. & Laird, B. B. Dielectric properties of organic solvents in an electric field. *J. Phys. Chem. C* **121**, 1025–1031 (2017).
33. Iermakova, D. I., Dugas, R., Palacín, M. R. & Ponrouch, A. On the comparative stability of Li and Na metal anode interfaces in conventional alkyl carbonate electrolytes. *J. Electrochem. Soc.* **162**, A7060 (2015).
34. Gao, L. *et al.* Revealing the chemistry of an anode-passivating electrolyte salt for high rate and stable sodium metal batteries. *J. Mater. Chem. A* **6**, 12012–12017 (2018).
35. Aurbach, D., Levi, M. D., Levi, E. & Schechter, A. Failure and stabilization mechanisms of graphite electrodes. *J. Phys. Chem. B* **101**, 2195–2206 (1997).